Extrinsic 6DoF Calibration of 3D LiDAR and Radar

Juraj Peršić, Ivan Marković, Ivan Petrović
University of Zagreb Faculty of Electrical Engineering and Computing
Department of Control and Computer Engineering
Unska 3, HR-10000, Zagreb, Croatia
Email: juraj.persic@fer.hr, ivan.markovic@fer.hr, ivan.petrovic@fer.hr

***Abstract*—Environment perception is a key component of any autonomous system and is often based on a heterogeneous set of sensors and fusion thereof, for which extrinsic sensor calibration plays fundamental role. In this paper, we tackle the problem of 3D LiDAR–radar calibration which is challenging due to low accuracy and sparse informativeness of the radar measurements. We propose a complementary calibration target design suitable for both sensors, thus enabling a simple, yet reliable calibration procedure. The calibration method is composed of correspondence registration and a two-step optimization. The first step, reprojection error based optimization, provides initial estimate of the calibration parameters, while the second step, fiel of view optimization, uses additional information from the radar cross section measurements and the nominal field of view to refine the parameters. In the end, results of the experiments validated the proposed method and demonstrated how the two steps combined provide an improved estimate of extrinsic calibration parameters.**

I. Introduction

Robust environment perception and inference is one of the essential tasks which an autonomous mobile robot or vehicle has to accomplish. To achieve this goal, various sensors such as cameras, radars, LiDAR-s, and inertial navigation units are used and information thereof is often fused. A fundamental step in the fusion process is sensor calibration, both intrinsic and extrinsic. Former provides internal parameters of each sensor, while latter provides relative transformation from one sensor coordinate frame to the other. The calibration can tackle both parameter groups at the same time or assume that sensors are already intrinsically calibrated and proceed with the extrinsic calibration, which is the approach we take in the present paper.

Solving the extrinsic calibration problem requires finding correspondences in the data acquired by intrinsically calibrated sensors, which can be challenging since different sensors can measure different physical quantities. The calibration approaches can be target-based or targetless. In the case of target-based calibration, correspondences originate from a specially designed target, while targetless methods utilize environment features perceived by both sensors. Former has the advantage of the freedom of design which maximizes the chance of both sensors perceiving the calibration target, but requires the development of such a target and execution of an appropriate offline calibration procedure. The latter has the advantage of using the environment itself as the calibration target and can operate online by registering structural correspondences in the environment, but requires both sensors to be able to extract the same environment features. For example, calibration of a 3D-LiDAR and a camera can be based on line features detected as intensity edges in the image and depth discontinuities in the point cloud [1]. In addition, registration of structural correspondences can be avoided by odometry-based methods, which use the system's movement estimated by individual sensors to calibrate them [2], [3]. However, for all practical means and purposes limited resolution of current automotive radar systems eliminates the feasibility of targetless methods, as the radar is virtually unable to infer the structure of the detected object and extract features such as lines or corners. Since an automotive radar is used in the present paper and we are targeting in situ calibration techniques, our approach will focus further on target-based methods.

Target-based 3D LiDAR calibration commonly uses flat rectangles which are easily detected and localized in the point cloud. For example, extensive research exists on 3D LiDAR-camera calibration with a planar surface covered by a chequerboard [4]–[7] or a set of QR codes [8], [9]. Extrinsic calibration of a 2D LiDAR-camera pair was also calibrated with the same target [10], while improvements were made by extracting centerline and edge features of a V-shaped planar target [11]. Furthermore, an interesting target adaptation to the working principle of different sensors was presented in [12], where the authors proposed a method for extrinsic calibration of a 3D LiDAR and a thermal camera by expanding a planar chequerboard surface with a grid consisting of light bulbs. Concerning automotive radars, common operating frequencies (24 GHz and 77 GHz) result with reliable detections of conductive objects, such as plates, cylinders, and corner reflectors, which are then used in intrinsic and extrinsic calibration methods [13]. In [14] authors used a metal panel as the target for radar-camera calibration. They assume that all radar measurements originate from a single ground plane, thereby neglecting the 3D nature of the problem. The calibration is found by optimizing homography transformation between the ground and image plane. Contrary to [14], in [15] authors do not neglect the 3D nature of the problem. Therein, they manually search for detection intensity maximums by moving a corner reflector within the field of view (FOV) of the radar. They assume that detections lie on the radar plane (zero elevation plane in the radar coordinate frame). Using these points a homography transformation is optimized between the radar and the camera. The drawback of this method is that the maximum intensity search is prone to errors, since the

return intensity depends on a number of factors, e.g., target orientation and radar antenna radiation pattern which is usually designed to be as constant as possible in the FOV. In [16] radar performance is evaluated using a 2D LiDAR as a ground truth with a target composed of radar tube reflector and a square cardboard. The cardboard is practically invisible to the radar, while enabling better detection and localization in the LiDAR point cloud. These complementary properties were taken as an inspiration for our target design.

While the above described radar calibration methods provide sufficiently good results for the targeted applications, they lack the possibility to fully assess the placement of the radar with respect to other sensors, such as a 3D LiDAR. Therefore, we propose a novel method which utilizes a 6 degrees of freedom (DOF) extrinsic calibration of a 3D LiDAR-radar pair. The proposed method involves target design, correspondence registration, and two-step optimization. The first step is based on reprojection error optimization, while the second step uses additional information from the radar cross section (RCS)—a measure of detection intensity. RCS distribution across the radar's FOV is used to refine a subset of calibration parameters that were noticed to have higher uncertainty.

II. 6DoF Extrinsic Radar-LiDAR Calibration

The proposed method is based on observing the calibration target placed at a range of different heights, both within and outside of the nominal radar FOV. It requires the 3D LiDAR's FOV to exceed the radar's vertical FOV, which is the case in most applications. In addition, due to the problems associated with radars such as ghost measurements from multipath propagation, low angular resolution etc., data collection has to be performed outdoor at a set of ranges ($2 - 10\,\mathrm{m}$) with enough clear space around the target. The proposed method consist of a careful target design, correspondence registration in the data from the sensors, and a two-step optimization procedure all elaborated in the sequel.

A. Calibration Target Design

Properties of a well-designed target are (i) ease of detection and (ii) high localization accuracy for both sensors. In terms of the radar, a target with a high RCS provides good detection rates. Formally, RCS of an object is defined as the area of a perfectly conducting sphere whose echo strength would be equal to the object strength [13]. Consequently, it is a function of object size, material, shape and orientation. While any metal will suffice for the material, choosing other properties is not trivial. Radars typically estimate range and angle of an object as a centroid in the echo signal. Therefore, in order to accurately localize the source of detection, the target should be as small as possible, but which implies a small RCS. Thus, a compromise between the target size and a high enough RCS has to be considered. Radar reflectors, objects that are highly visible to radars, are used not only in intrinsic calibration, but also as marine safety equipment resulting in numerous designs. Given the previous discussion, we assert that one of these designs can be considered as a good compromise and we

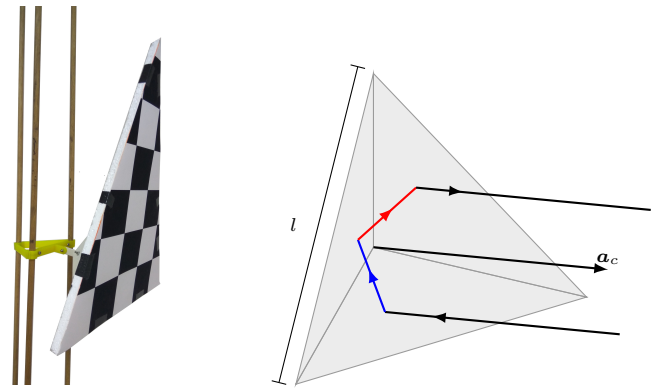

(a) Calibration Target (b) Corner reflector

Fig. 1: Constructed calibration target and the illustration of the working principle of the triangular trihedral corner reflector

chose the triangular trihedral corner reflector which consists of three orthogonal flat metal triangles.

The constructed radar calibration target and an illustration of the working principle is shown in Fig. 1a. It has an interesting property that any ray reflected from all three sides is returned in the same direction $\mathbf{a_c}$ as illustrated in Fig. 1b. The reason behind this is that normals of the three sides form an orthonormal basis. Namely, reflection causes direction reverse of incident ray's component parallel to the surface normal, while the component parallel to the surface tangent plane remains the same. After three reflections, which form an orthonormal basis, the ray's direction is reversed. Due to this property, regardless of the incident angle, many rays are returned to their source, i.e., the radar. Unlike a single flat plate, which has a high RCS but is highly sensitive to orientation changes, trihedral corner reflector provides a high and stable RCS. When the axis of the corner reflector, $\mathbf{a_c}$, points directly to the radar, it reaches its maximum value:

$$\sigma_c = \frac{\pi l^4}{3\lambda^2}. \tag{1}$$

Analytical description of the reflector RCS as a function of the orientation is nontrivial. However, from experiments presented in [13], it can be seen that orientation changes of $\pm 20^\circ$ result in a slight decrease of RCS, which can be approximated as a constant, while $\pm 40^\circ$ causes a decrease of $-3\mathrm{dBm}^2$. Furthermore, authors in [17] show that all the rays which go through multiple reflections travel the same length as the ray which is reflected directly from the corner centre. This results in a high localization accuracy.

Corner reflector is visible to the LiDAR, but is difficult to accurately localize at greater distances due to its small size and complex shape. This problem is solved by placing a flat styrofoam triangle board in front of the corner reflector. Styrofoam is made of approximately 98% air resulting with low permittivity (around 1.10) and nonconductiveness. These properties make it virtually invisible to the radar, but still visible to the LiDAR. However, instead of a common rectangular shape, we choose a triangular shape with which we

can solve localization ambiguity issues caused by finite LiDAR resolution. Namely, LiDAR azimuth resolution is commonly larger than the elevation resolution, which results with the 'slicing' effect of an object; thus, translating the rectangle along the vertical axis would yield identical measurements until it becomes visible to the next LiDAR layer (which is not the case for the triangle shape). This effect has a stronger impact on localization at greater distances which are required by our method.

Finally, target stand should be able to hold the target at a range of different heights (0–2 m). Additionally, it must have a low RCS not to interfere with the target detection and localization. We propose a stand made of three thin wooden rods which are fixed to a ground wooden plane and connected with a plastic bridge (Fig. 1a). Target attached to the bridge can be slided and tilted to adjust its height and orientation.

B. Correspondence Registration

Correspondence registration in the data starts with the detection of the triangle in the point cloud. The initial step is to segment plane candidates from which edge points are extracted. Afterwards, we try to fit these points to the triangle model. Levenberg–Marquardt (LM) algorithm optimizes the pose of the triangle by minimizing the distance from edge point to the border of the triangle model. A final threshold is defined based on which we accept or discard the estimate. Position of the corner reflector origin is calculated based on the triangle pose estimate and the known configuration of the target.

Radar data consists of a vector of detected objects described by the detection angle, range, range rate and RCS, which is for the i-th object in the radar coordinate frame, $\mathcal{F}_r : ({}^r x, {}^r y, {}^r z)$, designated as ${}^r\boldsymbol{m}_i = [{}^r\phi_{r,i}\ {}^r r_{r,i}\ {}^r\dot{r}_{r,i}\ {}^r\sigma_{r,i}]$. The only structural property of detected objects is contained within the RCS, which is influenced by many other factors; hence, it is impossible to classify a detection as the corner reflector based solely on the radar measurements. To find the matching object, a rough initial calibration is required, e.g., with a measurement tape, which is used to transform the estimated corner position from the LiDAR coordinate frame, $\mathcal{F}_l : ({}^l x, {}^l y, {}^l z)$, into the radar coordinate frame $\mathcal{F}_r$, and eliminate all other objects that fall outside of a predefined threshold. The correspondence is accepted only if a single object is left.

The radar correspondence points are obtained as follows. The target is observed for a short period while the registered correspondences fill a correspondence group. Variances of the radar data $({}^r\phi_{r,i}, {}^r r_{r,i}, {}^r\sigma_{r,i})$ within the group are used to determine the stability of the target. If any of the variances surpasses a threshold, the correspondence is discarded, since it is likely that the target detection was obstructed. Otherwise, the values are averaged. In addition, we create unregistered groups where radar detections are missing. These groups are used in the second optimization step where we refine the FOV.

Hereafter, we will refer to the mean values of the groups as radar and LiDAR measurements.

C. Reprojection Error Optimization

Once the paired measurements are found, alignment of sensor coordinate frames is performed. To ensure that the optimization is performed on the radar measurements originating from the calibration target, we perform RCS threshold filtering. We choose the threshold ζ_{RCS} lower than the σ_c so that we encompass as many strong and reliable radar measurements while leaving out the possible outliers.

The optimization parameter vector includes the translation and rotation part, i.e., $\boldsymbol{c}_r = [{}^r\boldsymbol{p}_l\ \boldsymbol{\Theta}]$. For translation, we choose position of the LiDAR in the radar coordinate frame ${}^r\boldsymbol{p}_l = [{}^r p_{x,l}\ {}^r p_{y,l}\ {}^r p_{z,l}]^T$. For rotation, we choose Euler angles representation $\boldsymbol{\Theta} = [\theta_z\ \theta_y\ \theta_x]$ where rotation from $\mathcal{F}_r$ to $\mathcal{F}_l$ is given by:

$$ {}^l_r R(\boldsymbol{\Theta}) = {}^l_2 R_x(\theta_x) {}^2_1 R_y(\theta_y) {}^1_r R_z(\theta_z). \tag{2} $$

Figure 2 illustrates the calculation of the reprojection error for the i-th paired measurement. As discussed previously, radar provides measurements in spherical coordinates lacking elevation ${}^r\boldsymbol{s}_{r,i} = [{}^r r_{r,i}\ {}^r\phi_{r,i}\ \sim]$, i.e., it provides an arc ${}^r a_{r,i}$ upon which the object potentially resides. On the other hand, LiDAR provides a point in Euclidean coordinates ${}^l\boldsymbol{x}_{l,i}$. Using the current transformation estimate, LiDAR measurement ${}^l\boldsymbol{x}_{l,i}$ is transformed into the radar coordinate frame:

$$ {}^r\boldsymbol{x}_{l,i}(\boldsymbol{c}_r) = {}^l_r R^T(\boldsymbol{\Theta}) \cdot {}^l\boldsymbol{x}_{l,i} + {}^r\boldsymbol{p}_l, \tag{3} $$

and then ${}^r\boldsymbol{x}_{l,i}$ is converted to spherical coordinates ${}^r\boldsymbol{s}_{l,i} = [{}^r r_{l,i}\ {}^r\phi_{l,i}\ {}^r\psi_{l,i}]$. By neglecting the elevation angle ${}^r\psi_{l,i}$, we obtain the arc ${}^r a_{l,i}$ upon which LiDAR measurement resides and can be compared to the radar's. Reprojection error $\epsilon_{r,i}$ is then defined as the Euclidean distance of points on the arc for which ${}^r\psi_{r,i} = {}^r\psi_{l,i} = 0°$:

$$ \epsilon_{r,i}(\boldsymbol{c}_r) = \left\| \begin{bmatrix} {}^r r_{r,i} \cos({}^r\phi_{r,i}) \\ {}^r r_{r,i} \sin({}^r\phi_{r,i}) \end{bmatrix} - \begin{bmatrix} {}^r r_{l,i} \cos({}^r\phi_{l,i}) \\ {}^r r_{l,i} \sin({}^r\phi_{l,i}) \end{bmatrix} \right\|. \tag{4} $$

Using the LM algorithm, we obtain the estimate of the calibration parameters $\hat{\boldsymbol{c}}_r$ by minimizing the sum of squared reprojection errors from N measurements:

$$ \hat{\boldsymbol{c}}_{\mathbf{r}} = \arg\min_{\boldsymbol{c}_r} \left(\sum_{i=1}^{N} \epsilon_{r,i}^2(\boldsymbol{c}_r) \right). \tag{5} $$

Optimization of described reprojection error yields unequal estimation uncertainty among the calibration parameters. Namely, translation in the radar plane and rotation around it's normal causes significant changes in the radar measurements. Therefore, parameters ${}^r p_{x,l}$,${}^r p_{y,l}$ and θ_z can be properly estimated. In contrast, the change in the remaining parameters ${}^r p_{z,l}$,θ_y and θ_x causes smaller changes in the radar measurements, e.g. translation of radar along ${}^r z$ introduces only a small change in the range measurement. Therefore, these parameters are refined in the next step.

Due to the data filtering in the previous steps, not many outliers are present in the data. The remaining outliers are removed from the data set by inspection of the reprojection error after the optimization. Measurements that surpass a

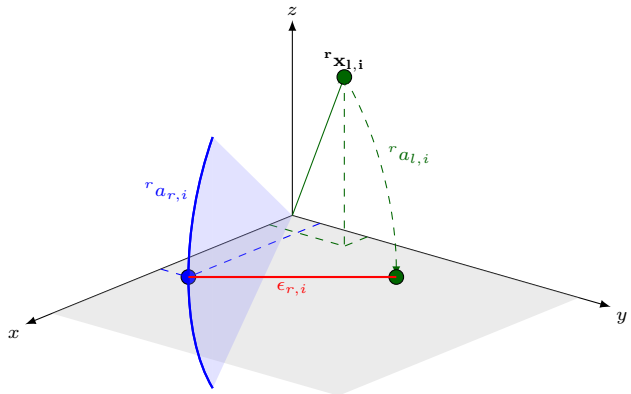

Fig. 2: Illustration of reprojection error calculation. Green indicates LiDAR measurement, blue radar's, while red shows reprojection error.

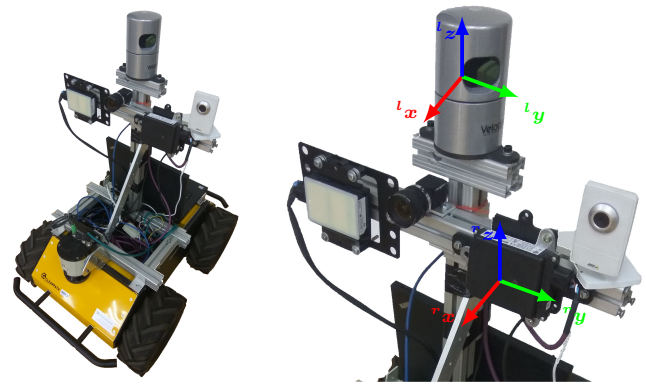

(a) Mobile robot (b) Sensor placement

Fig. 3: Mobile robot and sensors used in the experiment.

threshold are excluded from the dataset and optimization is performed again on the remaining measurements.

D. FOV optimization

To refine the parameters with higher uncertainty we propose a second optimization step which uses additional information from RCS. We try to fit the radar nominal FOV in the LiDAR data by encompassing as many measurements with high RCS as possible. Definition of RCS is such that it does not depend on the radiation of the radar. However, radar estimates the object RCS based on the intensity of the echo which is dependent on the radiated energy. Intrinsic calibration of a radar ensures that RCS is correctly estimated only within the nominal FOV where it is fairly constant. As the object leaves the nominal FOV, less energy is radiated in its direction, which then results in decrease of RCS until the object becomes undetectable. This effect is used to estimate the pose of the nominal FOV based on the RCS distribution across the LiDAR's data.

Vertical FOV of width $2\psi_f$ is defined with two planes that go through the origin of $\mathcal{F}_r$, $\mathcal{P}_U$ and $\mathcal{P}_D$, with elevation angles $\pm\psi_f$. We propose an optimization in which we position radar's nominal FOV, so that as many as possible strong reflections fall within it, while leaving the weak ones out. The optimization parameter vector consist of a subset of transformation parameters and an RCS threshold, $\boldsymbol{c}_f = [{}^r p_{z,l}\ \theta_y\ \theta_x\ \zeta_{RCS}]$, whereas other parameters are kept fixed.

After transforming a LiDAR measurement ${}^l\boldsymbol{x}_{l,i}$ to $\mathcal{F}_r$, the FOV error of i-th measurement $\epsilon_{f,i}$ is defined as:

$$\epsilon_{f,i}(\boldsymbol{c}_f) = \begin{cases} 0 & \text{if inside FOV and } \sigma_i > \zeta_{RCS} \\ d & \text{if inside FOV and } \sigma_i > \zeta_{RCS} \\ 0 & \text{if outside FOV and } \sigma_i < \zeta_{RCS} \\ d & \text{if outside FOV and } \sigma_i < \zeta_{RCS}, \end{cases} \tag{6}$$

where

$$d = \min\{\text{dist}(\mathcal{P}_U, {}^r\boldsymbol{x}_{l,i}), \text{dist}(\mathcal{P}_D, {}^r\boldsymbol{x}_{l,i})\}. \tag{7}$$

Error is greater than zero only if the LiDAR measurement falls inside the FOV when it should not according to the threshold, and vice versa. Function $\text{dist}(\mathcal{P}, x)$ is defined as an unsigned distance from plane $\mathcal{P}$ to point x.

An estimate of calibration parameters is obtained by minimizing the following cost function:

$$\hat{\boldsymbol{c}}_{\mathbf{f}} = \arg\min_{\boldsymbol{c}_f} \left(\sum_{i=1}^{N} \epsilon_{f,i}^2(\boldsymbol{c}_f) \right). \tag{8}$$

Dependence of the cost function is discrete with respect to the RCS threshold, since change of the threshold does not affect the cost function until at least one measurement at the edge falls in or out of the FOV. This results in many local minima and the interior points method was used for optimization, since it was found to be able to converge in majority of analysed cases.

III. Experiment Results

An outdoor experiment was conducted to test the proposed method. A mobile robot Husky UGV, shown in Fig. 3, was equipped with a Velodyne HDL-32E 3D LiDAR and two short range radars from different manufacturers, namely the Continental SRR 20X and Delphi SRR2.

Commercially available radars are sensors which provide high level information in the form of detected object list. Raw data, i.e., the return echo, is processed by proprietary signal processing techniques and is unavailable to the user. However, from the experiments conducted with both radars, we noticed that they follow the behaviour as expected from our calibration method. The only noticed difference is that the target stand without the target was completely invisible to Continental, while the Delphi was able to detect it at closer ranges (${}^r r_{r,i} < 5$ m). This effect was present because the Delphi radar accepts detections with lower RCS. However, this did not present an issue, because the stand has a significantly lower RCS than the target and it was easily filtered out. Since the purpose of the experiment is evaluation of the method and not radar performance, in the sequel we only present results for the Continental radar.

Continental radar technical properties of interest are given in Table I. Based on the analysis of the reprojection error,

TABLE I: Continental SRR 20X specifications

Continental SRR 20X	Value
HVOF × VFOV	150° × 12°
Range Accuracy	0.2m
Azimut Accuracy @ HFOV	±2°@±20°; ±4°@±60°; ±5°@±°75

radar measurements outside of the azimuth angle range of $\pm 45°$ were excluded from the reprojection error optimization, because they exhibited significantly higher reprojection errors than those inside the range. Considering FOV optimization, we noticed that outside of the azimuth angle range $\pm 60°$ radar detections were occasionally missing. Therefore, they were excluded from the FOV optimization.

The calibration target was composed of a corner reflector with side length $l = 0.32\,\mathrm{m}$ which has a maximum RCS of $\sigma_c = 18.75\,\mathrm{dBm}^2$. Based on vertical resolution of the Velodyne HDL-32E LiDAR (1.33°) we used styrofoam triangle of height $h = 0.65$ m. It ensured extraction of at least two lines from the target, which is a prerequisite to unambiguously determine the pose. Data acquisition was done by driving a robot in the area up to 10 m of range with target placed at 17 different heights ranging from ground up to 2 m height. In total, 880 registered radar-LiDAR measurements were collected, together with 150 LiDAR measurements unregistered by the radar.

A. Results

To asses the quality of calibration results we conducted four experiments. First, we examined the distribution of the reprojection error after both optimization steps and compared it to a 2D optimization, which minimizes reprojection error by optimizing only the calibration parameters with lower uncertainty, i.e., translation parameters ${}^r p_{x,l}$ and ${}^r p_{y,l}$, and rotation θ_z. Secondly, we inspect FOV placement with respect to the distribution of RCS over the LiDAR's data. Afterwards, we examine the correlation between RCS and the elevation angle. Lastly, we run Monte Carlo simulations by randomly subsampling the dataset to examine reliability of the estimated parameters and potential overfitting of data.

Parameters estimated by reprojection error optimization are $\hat{\boldsymbol{c}}_r = [-0.047, -0.132, 0.079\mathrm{m}; -2.07, 3.58, -0.02°]$, while FOV optimization estimates $\hat{\boldsymbol{c}}_f = [0.191, \mathrm{m}; 4.19, -0.84°; 12.85\mathrm{dBm}^2]$. In addition, a carefully measured translation by hand between the sensors ${}^r\tilde{\boldsymbol{p}}_l = [-0.08, -0.14, 0.18]^T$ m is given as a reference.

Figure 4 shows distribution of the reprojection error and is composed of three histograms, where we can see how the reprojection error of both steps of calibration is compared to the case of 2D calibration. We notice that neglecting the 3D nature of the problem causes higher mean and greater variance of the reprojection error which implies poor calibration. Furthermore, the FOV optimization is bound to degrade the overall reprojection error because it is not a part of the optimization criterium. However, resemblance between the distributions after the first and the second optimization steps implies low degradation of reprojection error.

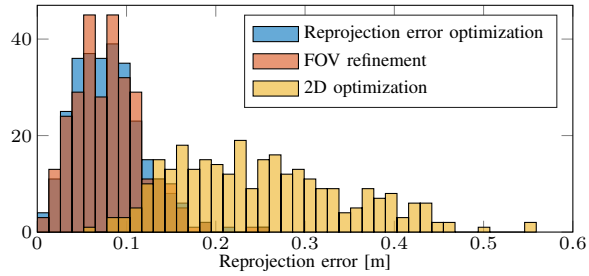

Fig. 4: Histogram of reprojection errors for the two steps of the calibration and the 2D calibration

TABLE II: Monte Carlo Analysis Results

	Reprojection Error Optimization	FOV optimization
${}^r p_{x,l}$	$\mathcal{N}(-0.047\mathrm{m},\ 1.53 \times 10^{-5})$	
${}^r p_{y,l}$	$\mathcal{N}(-0.132\mathrm{m},\ 6.12 \times 10^{-5})$	
${}^r p_{z,l}$	$\mathcal{N}(0.078\mathrm{m},\ 2.53 \times 10^{-3})$	$\mathcal{N}(0.174\mathrm{m},\ 9.10 \times 10^{-4})$
θ_z	$\mathcal{N}(-2.08°,\ 1.12 \times 10^{-2})$	
θ_y	$\mathcal{N}(3.59°,\ 9.50 \times 10^{-1})$	$\mathcal{N}(4.00°,\ 9.93 \times 10^{-2})$
θ_x	$\mathcal{N}(-0.03°,\ 8.08 \times 10^{-1})$	$\mathcal{N}(-0.93°,\ 1.44 \times 10^{-1})$

In Fig. 5, distribution of the RCS across LiDAR's data is shown. LiDAR's measuremenets are color-coded with the RCS of the paired radar measurement, accompanied with the black-dyed markers which indicate the lack of registered radar measurements. We can see that within the nominal FOV, target produces a strong, fairly constant reflections. As the elevation angle of the target leaves the radars FOV, the RCS decreases until the point where it is no longer detectable.

To examine the effect of decrease in the target's RCS as a function of the elevation angle after both optimization steps we use Fig. 6. It shows elevation ${}^r\psi_{l,i}$ of each LiDAR measurement transformed into the $\mathcal{F}_r$ and RCS of the paired radar measurement. In the ideal case, i.e. if the transformation was correct and the axis of corner reflector pointed directly to the radar in each measurement, the data would lay on the curve which describes radar's radiation pattern in respect to the elevation angle. The dispersion from the curve is present in the both steps due to the imperfect directivity of the target in the measurements. In addition, we notice a higher dispersion using only reprojection error optimization which indicates miscalibration.

Lastly, Monte Carlo analysis is done by randomly subsampling our dataset to half of the original size and performing 1000 runs of optimization on different subsampled datasets. The results follow a Gaussian distribution whose estimated parameters are given by the Table II. As expected, distributions of parameters ${}^r p_{x,l}$, ${}^r p_{y,l}$ and θ_z obtained by the reprojection error optimization have a significantly lower variance than the rest. Figure 7 ilustrates how the FOV optimization refines parameters ${}^r p_{z,l}$, θ_y and θ_x. We can see overall decrease in variance, as well as the shift in the mean. Estimation of parameter ${}^r p_{z,l}$ using reprojection error optimization is clearly further away from the measured value, unlike the FOV optimization's estimate.

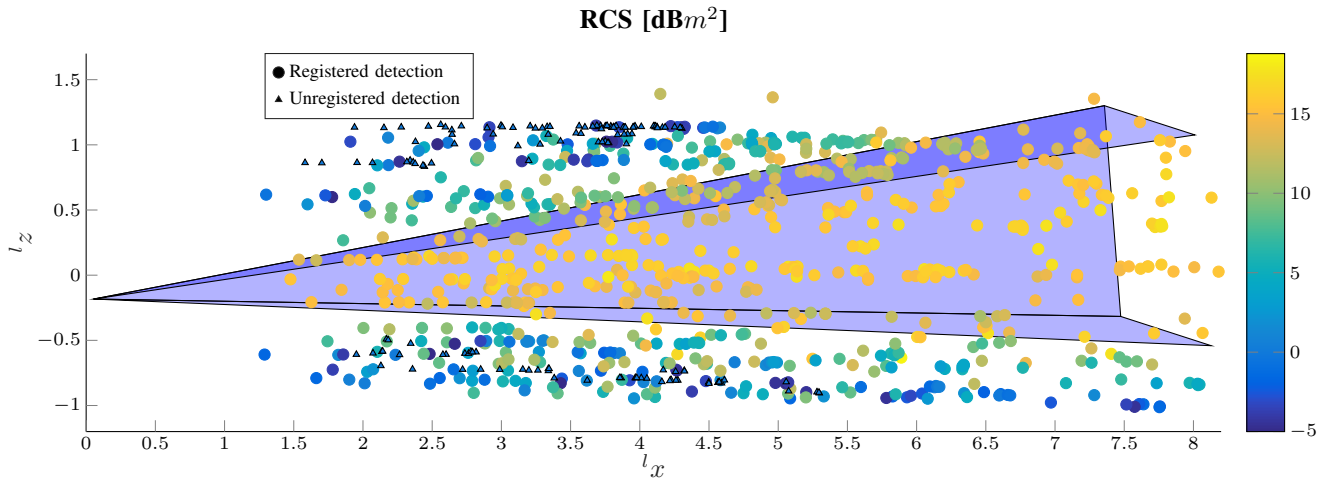

Fig. 5: RCS distribution across LiDAR 3D data and placement of the radar's FOV.

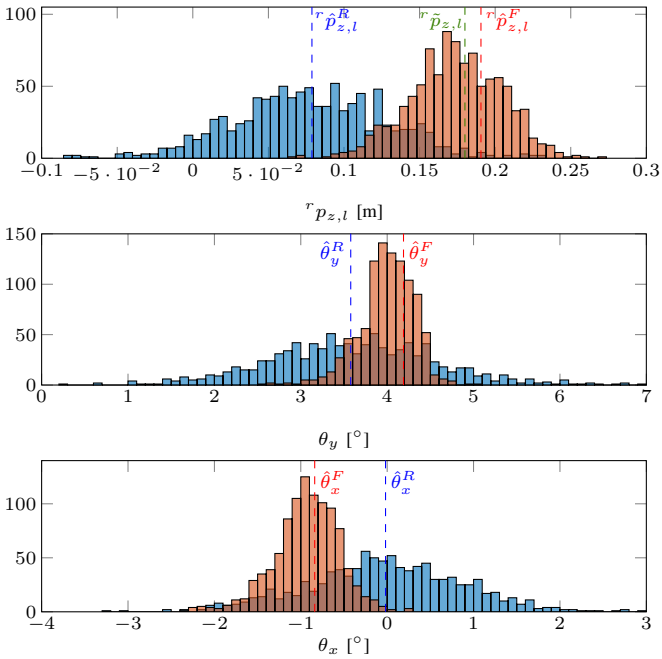

Fig. 7: Monte Carlo Analysis histograms. Red: calibration after reprojection error optimization; blue: with FOV optimization

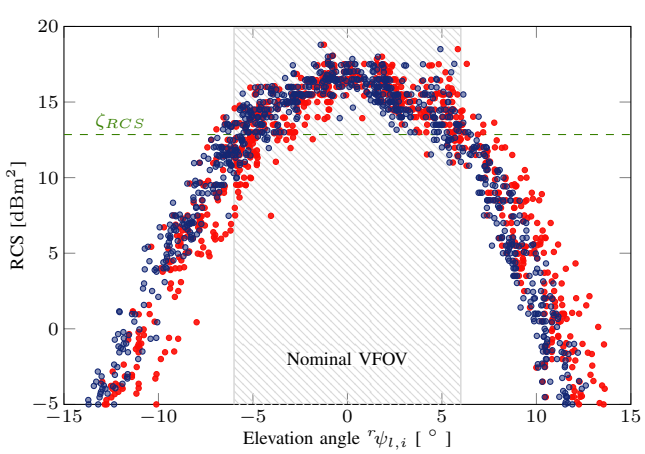

Fig. 6: RCS distribution across radar's VFOV. Red: calibration after reprojection error optimization; blue: with FOV optimization.

IV. Conclusion

In this paper we have proposed an extrinsic calibration method for a 3D-LiDAR-radar pair. A calibration target was designed in a way which enabled both sensors to detect and localize the target within their operating principles. The extrinsic calibration was found by a two-step optimization: (i) reprojection error optimization, which was the followed by (ii) FOV optimization which used additional information from RCS to refine the estimate of the calibration parameters. Results of the experiments validated the proposed method and demonstrated how the two steps combined provide an improved estimate of extrinsic calibration parameters.

References

[1] J. Levinson and S. Thrun, "Automatic Online Calibration of Cameras and Lasers," *Rss*, 2013.

[2] S. Schneider, T. Luettel, and H. J. Wuensche, "Odometry-based online extrinsic sensor calibration," *IEEE International Conference on Intelligent Robots and Systems*, no. 2, pp. 1287–1292, 2013.

[3] N. Keivan and G. Sibley, "Online SLAM with any-time self-calibration and automatic change detection," *Proceedings - IEEE International Conference on Robotics and Automation*, vol. 2015-June, no. June, pp. 5775–5782, 2015.

[4] G. Pandey, J. McBride, S. Savarese, and R. Eustice, "Extrinsic calibration of a 3D laser scanner and an omnidirectional camera," *IFAC Proceedings Volumes (IFAC-PapersOnline)*, vol. 7, no. PART 1, pp. 336–341, 2010.

[5] A. Geiger, F. Moosmann, O. Car, and B. Schuster, "Automatic camera and range sensor calibration using a single shot." *Icra*, pp. 3936–3943, 2012. [Online]. Available: http://dx.doi.org/10.1109/ICRA.2012.6224570%5Cnpapers3://publication/doi/10.1109/I

[6] M. Velas, M. Spanel, Z. Materna, and A. Herout, "Calibration of RGB Camera With Velodyne LiDAR," *Journal of WSCG no. 22*, pp. 135–144, 2014. [Online]. Available: http://www.fit.vutbr.cz/research/view_pub.php?id=10578

[7] L. Zhou and Z. Deng, "Extrinsic calibration of a camera and a lidar based on decoupling the rotation from the translation," *IEEE Intelligent Vehicles Symposium, Proceedings*, pp. 642–648, 2012.

[8] F. M. Mirzaei, D. G. Kottas, and S. I. Roumeliotis, "3D LIDAR-camera intrinsic and extrinsic calibration: Identifiability and analytical least-squares-based initialization," *Int. Journal of Robotics Research*, vol. 31, no. 4, pp. 452–467, 2012. [Online]. Available: http://www-users.cs.umn.edu/ stergios/papers/IJRR-2012-LidarCameraCalib.pdf

[9] J. L. Owens, P. R. Osteen, and K. Daniilidis, "MSG-cal: Multi-sensor graph-based calibration," *IEEE International Conference on Intelligent Robots and Systems*, vol. 2015-Decem, pp. 3660–3667, 2015.

[10] Q. Z. Q. Zhang and R. Pless, "Extrinsic calibration of a camera and laser range finder (improves camera calibration)," *2004 IEEE/RSJ International Conference on Intelligent Robots and Systems (IROS 2004)*, vol. 3, pp. 2301–2306, 2004.

[11] K. Kwak, D. F. Huber, H. Badino, and T. Kanade, "Extrinsic calibration of a single line scanning lidar and a camera," *IEEE International Conference on Intelligent Robots and Systems*, pp. 3283–3289, 2011.

[12] D. Borrmann, H. Afzal, J. Elseberg, and A. Nüchter, "Mutual calibration for 3D thermal mapping," *IFAC Proceedings Volumes (IFAC-PapersOnline)*, no. September, pp. 605–610, 2012.

[13] E. F. Knott, *Radar Cross Section Measurements.* ITP Van Nostrand Reinhold, 1993.

[14] T. Wang, N. Zheng, J. Xin, and Z. Ma, "Integrating millimeter wave radar with a monocular vision sensor for on-road obstacle detection applications," *Sensors*, vol. 11, no. 9, pp. 8992–9008, 2011.

[15] S. Sugimoto, H. Tateda, H. Takahashi, and M. Okutomi, "Obstacle detection using millimeter-wave radar and its visualization on image sequence," *Proceedings - International Conference on Pattern Recognition*, vol. 3, pp. 342–345, 2004.

[16] L. Stanislas and T. Peynot, "Characterisation of the Delphi Electronically Scanning Radar for Robotics Applications," *ARAA Australasian Conference on Robotics and Automation*, 2015. [Online]. Available: http://www.araa.asn.au/acra/acra2015/papers/pap167.pdf

[17] C. G. Stephanis and D. E. Mourmouras, "Trihedral rectangular ultrasonic reflector for distance measurements," *NDT&E international*, vol. 28, no. 2, pp. 95–96, 1995.